Combined physical and pharmacological anabolic osteoporosis therapies increase bone response and mechanoregulation in female mice

Authors: Friederike A. Schulte[1], Francisco C. Marques[1], Julia K. Griesbach[1], Claudia Weigt[1], Marcella von Salis-Soglio[1], Floor M. Lambers[1], Clemens Kreutz[2], Michaela Kneissel[2], Peter J. Richards[2,3], Gisela A. Kuhn[1], Ralph Müller[1]*

[1]Institute for Biomechanics, ETH Zurich; Zurich, Switzerland.

[2]Novartis Biomedical Research, Novartis Campus; Basel, Switzerland.

[3]Bone and Stem Cell Research Group, CABMM, University of Zurich; Zurich, Switzerland.

*Corresponding author. Email: ram@ethz.ch

Abstract: Bone's ability to adapt to mechanical demands is governed by mechanoregulation, the process by which cells sense and respond to mechanical stimuli to maintain skeletal integrity. In osteoporosis, increased bone resorption activity leads to structural deterioration and elevated fracture risk. While existing pharmacological therapies aim to restore bone mass to reduce fracture risk, it is unclear how they modulate mechanoregulation, especially when combined with physical interventions. Here, we investigate the joint effects of load-bearing physical and pharmacological treatment in a female mouse model of osteoporosis using longitudinal *in vivo* micro-computed tomography and computational mechanics. We demonstrate that mechanical loading additively and synergistically enhanced predicted strength, bone volume, and mechanoregulation parameters when combined with anabolic therapies (parathyroid hormone and sclerostin antibody) but not with anti-catabolic treatments (bisphosphonates). Increases in predicted strength are associated with reductions in bone resorption rates, shifts in the (re)modeling thresholds as anticipated by Frost in the mechanostat theory, and the modeling capacity of anabolic pharmacological treatments. These findings underscore the therapeutic potential of combining anabolic pharmacological therapies with load-bearing physical activity, particularly in early treatment phases, to optimize bone adaptation and fracture prevention in osteoporosis management.

Introduction

Postmenopausal osteoporosis in women is characterized by increased bone resorption, leading to structural deterioration of the bone micro-architecture and increased susceptibility to fractures[1]. Exercise is fundamental to bone health, but its role alongside pharmacological treatment remains an area of active inquiry[2]. Patients with diagnosed osteoporosis often question the compatibility of exercise with pharmacological treatment, some fearing interference with drug efficacy, others assuming that their potent medications obviate the need for physical activity. This highlights the need for evidence on whether mechanical loading improves outcomes for bone strength beyond pharmacological monotherapy.

Mechanical loads are transmitted from the organ to bone cells, where osteocytes act as mechanosensors, osteoblasts form, and osteoclasts resorb bone. This interplay drives both remodeling (formation followed by resorption) and modeling (formation without prior resorption), the latter potentially via lining cell redifferentiation in the absence of sclerostin[3]. Key signaling pathways between bone cells include Wnt/β-catenin[4] (osteocyte-osteoblast) and RANKL/OPG[5] (osteoblast-osteoclast). To study these dynamic processes *in vivo*, high-resolution imaging techniques such as micro-computed tomography (micro-CT) are commonly used. While micro-CT does not resolve individual cells or molecular signals, it captures the net microstructural changes resulting from formation and resorption, which are collectively referred to as bone (re)modeling[6].

On the cellular level, anti-resorptive bisphosphonates (BIS) prevent osteoclast attachment and activity by binding to hydroxyapatite crystals in the bone matrix, and are characterized by low osteoanabolic capacity[7]. We hypothesized that mechanical loading would stimulate bone formation, but bisphosphonates might blunt this response by inhibiting (re)modeling.

Intermittent parathyroid hormone (PTH) exerts anabolic effects by binding to PTH-receptors on osteoblasts and osteocytes, leading to suppression of sclerostin expression and subsequent activation of the Wnt/β-catenin signaling pathway. This promotes osteoblastic activity and indirectly enhances osteoclast recruitment via upregulation of RANKL expression by osteoblasts[8]. PTH and mechanical loading have shown synergistic effects in cortical bone[9, 10]. We hypothesized that in trabecular bone, their combination would suppress otherwise increased resorption, and concurrently stimulate bone formation[11].

Sclerostin antibodies (SclAB) inhibit a Wnt/β-catenin-signaling antagonist protein, promoting osteoblast activity and suppressing osteoclast activity[12]. Wnt/β-catenin-signaling is initiated when a Wnt ligand binds to a Frizzled family receptor and its co-receptor LRP5/6 on the surface of a cell, resulting in β-catenin stabilization and target gene transcription inside the cell[11]. We hypothesized mechanical loading in combination with SclAB would increase formation and decrease resorption further. Synergy may arise because mechanical loading downregulates sclerostin expression in osteocytes[13], while SclAB pharmacologically neutralizes it, amplifying the same pathway from two directions, especially in trabecular bone which particularly adapts its microarchitecture to mechanical demands. It should be noted that, similar to mechanical loading, sclerostin antibody effects saturate after a certain time, which limits their long-term use as a standalone therapy[14].

Frost's mechanostat theory[15, 16, 17] proposes that bone adapts to maintain mechanical strain within a defined setpoint range - much like a thermostat. The setpoints separate the four following states: the disuse state for bone resorption; the adapted state for quiescence, the overload state for formation, and the fracture state for microdamage and fractures. The mechanostat theory was introduced more than 30 years ago. In this theoretical construct, anti-catabolic bisphosphonates help inhibit increased bone resorption in underloaded areas by raising the mechanical setpoints towards higher strains. Anabolic treatments theoretically

promote bone formation by lowering the mechanical setpoints required to initiate formation, provided mechanical loading is also encouraged. Measuring the "setpoints" of osteoporosis medications in the context of Frost's mechanostat theory, however, is not straightforward, as the setpoints themselves are theoretical constructs that describe the mechanical thresholds at which bones adjust their structure, and measuring them experimentally would require complex assessments of both bone volume and mechanical strain under highly controlled conditions.

Here we provide experimental insights into this interaction using *in vivo* micro-computed tomography (micro-CT) and finite-element modeling in a C57BL/6 mouse model of osteoporosis. The aim of this study was to explore whether combining pharmacological treatments with mechanical loading leads to improved pharmacological treatment outcomes, i.e. stronger bones. We tested short-term effects of BIS, PTH, and SclAB treatment with or without mechanical loading of the 6th caudal vertebra, aiming to maximize bone accrual in early treatment phases. The choice of selected therapies was based on clinical relevance and distinct modes of action in the bone (re)modeling process.

Results

Micro-architectural and (re)modeling differences reveal treatment-specific effects on bone recovery after ovariectomy

As shown in Fig. 1a, C57BL/6 mice were ovariectomized at 15 weeks-of-age, and bone loss was confirmed in all animals (n=105) via *in vivo* micro-CT of the 6th caudal vertebra (-26.8 ± 0.95% change in bone volume fraction (BV/TV) from baseline). From week 20 to 24, animals received pharmacological and/or mechanical treatment through an established tail vertebra loading model[18].

109 In the VEH-group, BV/TV continued to decline from week 20, while all monotreatment groups
110 showed significant increases after four weeks of treatment ($p<0.001$, Fig. 1b). Trabecular
111 thickness (Tb.Th) did not increase significantly in BIS compared to VEH, whereas all anabolic
112 treatments led to increases, but lower in PTH than in ML and SclAB ($p<0.01$, Fig. 1c).
113 Trabecular number (Tb.N) was preserved in BIS but was significantly lower in all other groups
114 compared to BIS ($p<0.001$, Fig. 1d). Connectivity density (Conn.D) was preserved in BIS and
115 PTH and declined in VEH, ML, and SclAB ($p<0.05$, Fig. 1e). A full summary of these
116 microstructural parameters is provided in Supplementary Table S.2. As previously described[18],
117 mechanical loading increases BV/TV mainly through trabecular thickening despite a reduction
118 in trabecular number, explainable by a full loss of thin trabeculae - a pattern also seen in the
119 SclAB-group (Fig. 1c,d). In contrast, PTH increased BV/TV through moderate thickening and
120 sustained preservation of trabecular number, resulting in a smaller loss of connectivity. BIS
121 maintained BV/TV by preserving existing trabeculae, including thinner ones, with minimal
122 thickening (Fig. 1, b-e).

123 The micro-architectural changes resulted from the time course of formation and resorption (Fig.
124 1f). In week interval w20-22 (see also Supplementary Table S.5 for results from the second
125 interval, w22–24), bone formation rate per bone volume (BFR) was significantly increased in
126 ML and PTH compared to VEH, with no significant increases in BIS or SclAB (Fig. 1g).
127 Mineral apposition rate (MAR) did not differ between groups (Fig. 1h), while mineralizing
128 surface per bone surface (MS) was elevated in all treatment groups compared to VEH ($p<0.05$,
129 Fig. 1i). Bone resorption rate per bone volume (BRR) was significantly reduced in all treatment
130 groups versus VEH (Fig. 1j), where BRR in PTH was the least reduced (significantly higher
131 than VEH, ML, and BIS), consistent with the known anabolic effects of intermittent PTH
132 treatment. Surprisingly, BRR was found to be significantly lower than VEH, while not as low
133 as in ML and BIS. This decrease, even more pronounced in the second time interval (see

Supplementary material Table S.5), may result from micro-CT missing parts of the reversal phase between resorption and formation, thus potentially underrepresenting remodeling at the same sites. As expected, mineral resorption rate (MRR) was significantly lower in the BIS-group compared to VEH and unchanged in the anabolic groups (Fig. 1k), suggesting bisphosphonates preserve Tb.N (Fig. 1d) by preventing full trabecular resorption. Eroded surface per bone surface (ES), reflecting the proportion of bone surface previously affected by resorption, was significantly lower in ML and SclAB compared to VEH, BIS, and PTH ($p<0.05$, Fig. 1l).

Together, these results confirm that each monotherapy exerted effects consistent with its known mode of action - bisphosphonates preserving trabecular structure by suppressing bone resorption, and anabolic agents increasing bone mass predominantly through formation - while also highlighting treatment-specific differences in trabecular architecture and dynamic turnover.

Mechanical loading modulates structural and functional responses to pharmacological interventions

We next assessed how additional mechanical loading influenced the response to pharmacological treatment. In the BIS + ML-group, BV/TV gains were significantly less than the expected additive effects (treatment:loading: $p<0.05$, Fig. 2a), and did not differ significantly from BIS alone (Supplementary Table S.2). In contrast, anabolic treatment combined with mechanical loading (PTH + ML, SclAB + ML) resulted in additive increases, as supported by a non-significant treatment:loading interaction (Fig. 2a). ΔTb.Th was significantly higher in all combination groups compared to monotreatments after four weeks (Fig. 2b). ΔTb.N was preserved in BIS + ML, despite the known Tb.N loss with ML alone (Fig. 2c), suggesting BIS blunted this effect. The loss of Tb.N observed in SclAB was not rescued in

159 SclAB + ML (Fig. 2c). Conn.D as a measure of the structural integrity and interconnectedness
160 of the trabecular network, was preserved the most in BIS + ML, and PTH + ML (Fig. 2d). It
161 should be noted that structural parameters such as Tb.Th and Tb.N are interdependent; apparent
162 increases in Tb.Th may arise from the loss of complete thinner trabeculae. Synergy was found
163 in total area (Tt.Ar), leading to additive increases in cortical area fraction (Ct.Ar/Tt.Ar) and
164 cortical thickness (Ct.Th), found in Supplementary Fig. S.1 and Table S.4. Predicted strength
165 increased in all treatment groups, with loading-induced increases being additive in the PTH +
166 ML group and synergistic in the SclAB + ML group ($p<0.05$, Fig. 2e). Strain energy density
167 (SED) decreased in all treatment groups, being most pronounced in the combination groups,
168 with less than the expected additive reduction in BIS + ML (treatment:loading: $p<0.05$, Fig. 2f,
169 Table 1). Illustrating the effect of decreasing SED, the visualization of the 6th caudal vertebra
170 in a SclAB + ML animal shows a highly loaded trabecula at week 20, followed by structural
171 reorganization and reduced SED at week 24 (see Fig. 2g). Linear regression analysis revealed
172 that the changes in predicted strength did not correlate with baseline BV/TV ($R = 0.010$) and
173 moderately with Tb.Th ($R = 0.424$, Fig. 2h), indicating that initial BV/TV or Tb.Th serve as
174 poor or only moderate predictors of future changes in strength.

175

176 **Combination treatments affect bone formation and resorption dynamics differentially**

177 Bone formation rate per bone volume (BFR) was lowest in VEH and highest in the anabolic
178 combination groups ($p<0.05$, Fig. 3a). MAR showed synergy in SclAB + ML
179 (treatment:loading: $p<0.05$, Fig. 3b). MS increased additively in PTH + ML and SclAB + ML,
180 and antagonistically in BIS + ML (treatment:loading: $p<0.01$, Fig. 3c). Bone resorption rate per
181 bone volume (BRR) was reduced in all treatment groups ($p<0.05$, Fig. 3d). In BIS + ML, the
182 BRR reduction was antagonistically affected by mechanical loading (treatment:loading,
183 $p<0.05$). In contrast, BRR decreased synergistically in PTH+ML (treatment:loading: $p<0.05$,

Fig. 3d) and additively in SclAB + ML (Fig. 3d). MRR remained suppressed in BIS + ML and was unaffected by mechanical loading (Fig. 3e). ES decreased synergistically in PTH + ML treatment:loading: $p<0.05$, Fig. 3f) and SclAB + ML (treatment:loading: $p<0.01$, Fig. 3f). This synergistic effect was, at least in SclAB + ML, still present in the second time interval (see Supplementary Fig. S.2 and Table S.5 for results from w22–24). Representative trabecular microstructures and insets of the combination groups at both time intervals are depicted in Fig. 3g. Changes in predicted strength correlated linearly with BFR ($R = 0.830$) and decayed according to a power-law relationship with BRR ($\rho = 0.760$), indicating that small reductions in bone resorption rates under treatment can result in large increases in predicted strength (Fig. 3h).

Bone formation and resorption occur in mechanically distinct strain windows

To address the question whether pharmacological treatments target bone (re)modeling to the places that mechanically need it, we correlated the underlying mechanical signals in the trabecular compartment with subsequent formation and resorption events. Visually, spatial agreement was found between high SED and regions of subsequent bone formation, and low SED and regions of subsequent bone resorption (Fig. 4a). Quantitative analysis (Fig. 4b) showed that mean SED was significantly higher at formation sites ($p<0.05$) and significantly lower at resorption sites ($p<0.05$) compared to quiescent surfaces, when presented as percentage change to the average quiescent SED across all animals per group. The addition of mechanical loading to the monotreatments resulted in marginal changes, indicating that bone formation and resorption continue to occur in mechanically distinct strain windows despite possible influences of pharmacological interventions. Levene's test revealed significantly smaller variances between BIS and BIS + ML and between VEH and ML ($p<0.05$), indicative of more consistent mechanosensitive responses in these groups in the presence of mechanical loading.

209 Conditional probabilities of formation, quiescence, and resorption events for a given SED-value
210 were calculated and fitted with exponential functions. The probability for bone formation
211 increased with increasing SED, and the probability for bone resorption decreased with
212 increasing SED (Fig. 4c, Supplementary Fig. S.3 and Table S.6 for results in w22-24).
213 Especially the PTH + ML and SclAB + ML conditional probability curves opened up compared
214 to their monotreatments, indicating a higher responsiveness to mechanical signals (Fig. 4c). The
215 asymptotic resorption probability value min_R represents the point at which further increases in
216 local mechanical loading stimulus do not further suppress bone resorption. This value was
217 significantly lower in ML, PTH + ML, and in SclAB + ML than in VEH ($p<0.05$, Fig. 4d, Table
218 S.8). Further comparisons of the coefficients from fitted functions to the conditional
219 probabilities are provided in Supplementary Tables S.7 and S.8. The presence of few significant
220 differences between groups suggests mechanosensitivity of the system is largely preserved
221 regardless of the presence or absence of mechanical loading. Combined anabolic treatments
222 resulted in higher correct classification rate (CCR) values compared to VEH and the BIS groups
223 (Fig. 4e), with CCR being a metric used to evaluate the accuracy of classifying local bone
224 formation or resorption events based on predicted mechanical signals. However, CCR only
225 correlated moderately with the increases in strength, indicating increased mechanosensitivity
226 of the system may not fully explain the ability of bone to increase strength (Fig. 4f).

227

228 **Frost's mechanostat setpoints are shifted towards lower values for mono- and combined**
229 **treatments**

230 To assess potential shifts in the setpoints due to different drug or combination treatments,
231 (re)modeling velocity (RmV) curves and mechanostat parameters[19] were calculated for each
232 treatment group as an approximation to the mechanostat theory. These curves show the net
233 RmV for a given surface effective strain, where a negative value means net resorption and a

positive value means net formation (Fig. 5a). From these curves, formation saturation levels (FSL), resorption saturation levels (RSL), and (re)modeling thresholds (RmTs) were derived.

FSL was increased in all treatments compared to VEH ($p<0.001$, Fig. 5b, Supplementary Table S.9), and was significantly higher in anabolic combination groups compared to the respective monotreatments ($p<0.001$). This suggests an increased mechanosensitivity of the cells involved in bone formation. RSL was increased in the BIS and all combination groups compared to VEH ($p<0.05$, Fig. 5c). The increase in RSL under bisphosphonate treatment may be explained by the suppression of bone turnover: at comparable strain levels, resorption would typically occur, resulting in a lower RSL; however, due to inhibited osteoclast activity, this resorptive response is blunted, making the system appear saturated at a higher RSL value. Regarding the role of additional mechanical loading, only the PTH + ML group showed a significant increase compared to PTH alone ($p<0.05$, Supplementary Table S.9). This suggests that, under strain conditions that would typically lead to bone resorption, the balance has shifted towards bone formation. RmT values, representing the setpoints in the mechanostat theory, were decreased in all pharmacological treatment groups compared to VEH ($p<0.05$), with no significant improvements observed in the combination groups receiving mechanical loading (Fig. 5d). These results were even more pronounced in the second time interval (Supplementary Fig. 4d, Table S.9). The reduction in RmT suggests an upregulation of osteocytic mechanosensitivity, an expected outcome in the anabolic treatment groups, but an unexpected finding in the bisphosphonate-treated groups. This may reflect a compensatory osteocytic response to the suppressed bone resorption induced by bisphosphonate treatment. Furthermore, FSL correlated strongly with predicted strength increases ($R = 0.888$), while RmT exhibited a moderate inverse correlation ($\rho = 0.609$) when fitted with a power-law function. These findings suggest that a reduction in RmT may be a prerequisite for strength gains; however, actual increases in strength require anabolic potential (Fig. 5e,f).

The amount of modeling correlates highly with increases in predicted strength for all treatments

Next, we distinguished between the remodeling and the modeling ability of the different treatments. Visually, in several areas in VEH, high SED values decreased over time, but in other areas they increased and the resorption of a single trabecula led to a more heterogeneous SED distribution (Fig. 6a). While SED on average decreased over time for BIS + ML, this did not particularly affect areas with high SED, as there remained several highly strained areas in week 24. In contrast, both PTH + ML and SclAB + ML showed large decreases in SED, especially in areas with high SED values in week 20 (Fig. 6a).

The remodeling ability - as represented by the amount of resorption followed by formation - was in BIS, BIS + ML, PTH and SclAB comparable to VEH, and significantly lower in ML and the anabolic combination groups compared to VEH ($p<0.05$, Fig. 6b). In contrast, the modeling ability was significantly higher compared to VEH in all but the BIS group, with the highest amount in the anabolic combination treatments ($p<0.001$, Fig. 6c). Both remodeling and modeling capacity showed antagonistic effects in BIS + ML and additive effects in anabolic combination treatments (Fig. 6b,c). Remodeling showed a moderate inverse correlation with increases in predicted strength when fitted with a power-law function ($\rho = 0.476$, Fig. 6d), while modeling correlated strongly in a linear fit ($R = 0.928$, Fig. 6e). Fig. 6f illustrates the distribution of surface events relative to increasing effective strain. Remodeling events appeared strain-independent, and modeling increased with higher mechanical stimuli, particularly in the anabolic combination groups (Fig. 6f). There is also a non-linear increase in modeling with mechanical loading in comparison to the mono-treatment, with a stronger effect for low effective strain regions, especially for SclAB. Fig. 6g summarizes the trabecular bone response across treatments. Bisphosphonates, alone or with mechanical loading, help preserve trabecular

interconnectedness. Anabolic treatments combined with mechanical loading effectively enhance predicted strength by promoting formation and suppressing resorption. These additive effects across parameters likely underlie the observed synergistic gains in predicted strength, at least in SclAB.

Discussion

The main goal of osteoporosis therapy is to restore bone mass to reduce fracture risk. To achieve this efficiently, existing bone must be preserved and new bone formed at mechanically relevant sites. In healthy bone, bone (re)modeling is proposed to be regulated via the mechanostat[6, 19, 20, 21]. Here, we investigated how three current pharmacological treatments influence this regulation in the initial treatment phases in osteoporotic mice, particularly when combined with mechanical loading. Our findings suggest that all three investigated treatments induce bone formation and inhibit bone resorption at the mechanically relevant sites, but it was only in anabolic therapies that mechanical loading additively (PTH) or synergistically (SclAB) enhanced predicted bone strength.

When combined with sclerostin antibody treatment, mechanical loading led to a synergistic increase in predicted bone strength and an additive increase in bone volume fraction. Mineral apposition rates and reductions in eroded surfaces were synergistic, consistent with previous findings[12, 22, 23]. This response may be explained by dual suppression of the activity of sclerostin, a protein secreted by osteocytes that antagonizes Wnt signaling[11]. While mechanical loading independently suppresses sclerostin expression in osteocytes[13], SclAB pharmacologically neutralizes any residual sclerostin[11]. Together, these effects enhance Wnt/β-catenin activity, and likely contribute to the pronounced anabolic response[24]. Additional pathways may also be involved, as suggested by studies in SOST-KO mice, which still showed loading-induced bone formation[25]. One candidate is Dickkopf-1 (Dkk1), another Wnt inhibitor[26, 27, 28]. Robling et al.[13]

309 reported that mechanical loading reduced both *Sost* mRNA (-73%) and *Dkk1* (-49%) transcripts.
310 Since both proteins compete at LRP5/6 receptors in osteoblasts and osteocytes, their
311 simultaneous inhibition may underlie the observed synergy between SclAB and mechanical
312 loading.

313 We found additive increases in predicted strength and increased sensitivity of
314 mechanoregulation mechanisms for PTH + ML, which is in line with previous results where
315 PTH increased the mechanoresponse of osteoblasts only when combined with fluid flow[29].
316 Hagino et al.[30] hypothesized that PTH lowers the (re)modeling threshold of the (re)modeling
317 velocity function, which our findings support (Fig. 5). In previous animal studies, mechanical
318 loading combined with intermittent PTH (1-34) treatment led to synergistic effects in the
319 trabecular compartment of the healthy tibia, but it was only prevalent in regions that were not
320 remodeled, but modeled[31].

321 Bisphosphonates were the only treatment that preserved Tb.N but showed no additive effects
322 with mechanical loading, consistent with clinical studies reporting limited benefit of combining
323 bisphosphonates and exercise[32, 33]. Since mineralizing surface was significantly increased in the
324 bisphosphonate group compared to the vehicle group, our results suggest that bisphosphonates
325 not only affect the activity of osteoclasts but also that of osteoblasts, possibly through disruption
326 of the coupling process via elevated osteoclast apoptosis[34], potentially impairing the spatial
327 guidance of osteoblasts by the mechanical signal. The observation that the BIS and BIS+ML
328 groups exhibit RmT values as low as other treatment groups despite showing the least overall
329 remodeling response may indicate a compensatory increase in osteocytic mechanosensitivity,
330 potentially allowing selective resorption of mechanically less relevant areas.
331 This study focuses on osteoblast and osteoclast surface activities using *in vivo* micro-CT, which
332 allows longitudinal tracking of bone (re)modeling. Histological analysis could offer further
333 insight into cellular and tissue-level mechanisms to support the cell-specific interpretations

derived from the micro-CT data. However, due to the method of tissue preservation and the limited number of available samples, it was not considered feasible in the current study. It's worth noting though that previous work demonstrated a significant correlation between micro-CT-derived and histomorphometry-based MS and MAR ($R \approx 0.59 - 0.78$)[35, 36]. Furthermore, Birkhold et al.[37] have demonstrated the ability of longitudinal *in vivo* micro-CT to reliably quantify bone (re)modeling, i.e. separation into modeling and remodeling, in both trabecular and cortical bone. While *in vivo* micro-CT does not allow direct visualization of osteocytes, our measurements reflect the functional output of the bone cells in which osteocytes play an important role through orchestration of bone formation and resorption in response to local mechanical stimuli[6].

Regions with high local strain are linked to higher occurrences of microscopic tissue damage[38] of which even small amounts can lead to large reductions in strength[39] and increase fracture risk[40]. Reductions in strain energy density (SED) over time do not necessarily imply a decrease in bone formation capacity but rather reflect system saturation, consistent with mechanostat theory, where bone formation plateaus once strain thresholds are reached.

As a limitation, our developed system does not yet incorporate the level of the transcriptome[41]. Other cell types, particularly immune cells and endothelial cells, also contribute to bone (re)modeling via inflammatory signaling and vascularization, respectively. Recent work originating from fracture healing highlights the role of immune and vascular interactions, particularly in the context of aging and mechanical loading[42]. While these cell types were not analyzed here, future multimodal approaches could complement imaging-based assessments.

Given the biological differences among the therapies selected, including administration routes and duration limitations, direct long-term comparisons are not the aim of this study. Instead, our focus on short-term effects aimed to investigate potential synergistic improvements in bone strength and to gain mechanistic insight into how pharmacological and mechanical stimuli

359 modulate mechanoregulation. The findings support mechanostat theory: treatments lower
360 mechanical setpoints, enabling bone formation at lower strains. However, only anabolic
361 treatments effectively reinforce highly loaded trabeculae and reduce peak strains, underscoring
362 the importance of modeling capacity for strength gains. And while our results highlight the
363 promise of mechanical loading as an adjunct to anabolic therapies, clinical studies will
364 ultimately be required to determine optimal exercise modalities, just as pharmacological dosing
365 requires careful optimization.

366 In conclusion, the current study revealed that drug treatments target trabecular bone
367 (re)modeling at mechano-functionally relevant places, and osteoanabolic treatments in
368 combination with mechanical loading additively and synergistically increased the bone
369 response. The additive (PTH) and synergistic (SclAB) increases in predicted strength can be
370 explained by reductions in resorption rates, shifts in the (re)modeling thresholds as described
371 by Frost in the mechanostat theory more than 30 years ago, and by the modeling ability of
372 anabolic treatments. Being able to link organ-level changes induced by physical or
373 pharmacological therapies to the mechanosensitivity of the cells provides information on how
374 well skeletal structures can adapt to mechanical demands under pathological or treatment
375 conditions, a task for which the body has optimized itself over millions of years of evolution.
376 Load-bearing exercise may represent a promising adjunct option for physically active
377 osteoporosis patients on osteoanabolic therapy.

378

379 # Methods

380 **Study design**

381 The study design is illustrated in Fig. 1a. In total, 120 female 15-week-old C57BL/6 mice
382 (n=60, C57BL/6JRccHsd, RCC/Harlan; Füllinsdorf, Switzerland/ Horst, The Netherlands;

n=60, C57BL/6JRj mice (Janvier Labs, Le Genest-Saint-Isle, France) were subjected to bilateral ovariectomy. A basal micro-CT image of the 6th caudal vertebra was obtained (vivaCT 40, Scanco Medical, Brüttisellen, Switzerland). Recovery lasted five weeks after surgery, as in this period, an osteopenic state was established in the trabecular compartment of the 6th caudal vertebra in a previous study[43]. Pinning of the adjacent vertebrae as preparation for the loading procedure took place in week 17. At week 20, the animals were divided into 8 groups and the following treatments were administered for the following four weeks: BIS (n=9), BIS + ML (n=9), PTH (n=10), PTH + ML (n=9), SclAB (n=9), SclAB + ML (n=8), ML (n=26), VEH (n=25). 10 mice were excluded due to swollen tails or loose pins. In the SclAB study, 4 mice showed a periosteal reaction, possibly due to injury of the periosteum during intravenous injection at the tail vein. One mouse in the BIS + ML group did not lose bone volume after ovariectomy. These mice were excluded from evaluation, resulting in 105 animals included. Micro-CT was performed in weeks 15, 20, 22 and 24. Surgeries, imaging, and loading were performed under isoflurane anesthesia (induction 4%, maintenance 1.5-2.5%, Attane, Piramal Healthcare, India). Vehicle control was an isotonic buffer (pH 5.3). While the data was gained in four experiments (at different times), study and loading parameters were not different except for the administered pharmacological treatments, thus combined in this study. The bone responses of the VEH and the ML groups of both mouse lines (JRccHsd and 6JRj) showed no differences in reactions ($\Delta BV/TV_{w20-24;}$ VEH: $p = 0.937$; ML: $p = 0.206$; two-way ANOVA followed by Tukey's post-hoc test), thus ML groups from all experiments and VEH groups from all experiments were merged, explaining the larger sample size in these groups. The merging was conducted because separate vehicle group presentations would not have yielded additional insights but substantially would have increased data complexity (see Supplementary Table S.3). All animal experiments were performed with approval of the local authority (Kantonales Veterinäramt Zürich, Zurich, Switzerland, license number 171/2008, 108/2011, 078/2012) and reported according to ARRIVE 2.0 guidelines.

409 **Animal care and monitoring**

410 Animals were kept in groups of 3-5 mice in filter top cages in Scantainers (Scanbur, Karslunde,
411 Denmark) with *ad libitum* access to tap water and chow (KLIBA NAFAG 3437, Granivit AG,
412 Kaiseraugst Switzerland), wood chips bedding and a 12h:12h light:dark cycle. Room
413 temperature was 22 ± 2 °C and humidity was not controlled. Cages were changed weekly by
414 the experimenters. Microbiological status of the facility (Animal Imaging Center, ETH Zurich)
415 was not monitored, because it housed only animals during experiments. Animals were checked
416 and scored daily for three days after OVX surgery and pinning and at least three times per week
417 during the further experiment. Meloxicam 2 mg kg^{-1} was injected s.c. for three days after OVX
418 and pinning.

419

420 **Mechanical loading**

421 A validated *in vivo* mouse tail loading model was used to induce trabecular bone adaptation
422 under controlled mechanical conditions[43, 44, 45]. Stainless steel pins were implanted into adjacent
423 vertebrae under fluoroscopic guidance three weeks prior to loading. An 8N cyclic axial load
424 (3000 cycles, 10 Hz) was applied to the 6th caudal vertebra (CV6) using a custom loading device
425 (caudal vertebra axial loading device, CVAD[44]) three times a week. Control animals (0N
426 groups) underwent identical procedures, including pin placement and anesthesia but no load
427 was applied. A force of 8 N was used in order to maximize the effect within a short timeframe.
428 It was the maximum force that could be applied based on what the pins within the bone could
429 bear, and represents twice the force exerted on mouse vertebrae under physiological
430 conditions[46]. Pistoia simulations estimate a maximum failure load of 24.5 N at CV6 in
431 osteoporotic mice at week 20 (predicted trabecular strength, see Table S.2).

432

433 **Pharmacological treatment**

434 The BIS group received 100 µg kg^{-1} zoledronate (Zometa 4 mg/5 ml; Novartis Pharma Schweiz
435 AG, Bern) subcutaneously once in week 20. Corresponding VEH (0.9% NaCl, B. Braun
436 Medical AG, Switzerland) was injected at the same time point. Mice in the PTH study received
437 40 µg kg^{-1} PTH (hPTH 1-34, Bachem AG, Switzerland) or the according VEH (0.9% NaCl)
438 subcutaneously daily over four weeks. SclAB (100 mg kg^{-1}, Novartis Pharma AG, Basel,
439 Switzerland) or the corresponding VEH (isotonic buffer, pH 5.3) was injected i.v. weekly into
440 the lateral tail vein over 4 weeks.

441 BIS and SclAB doses were selected based on established protocols in the literature[24, 47]. The
442 PTH dose was determined in a dose-response study comparing 10 µg kg^{-1} d^{-1} and 40 µg kg^{-1} d^{-}
443 ^{1}, following an initial 80 µg kg^{-1} d^{-1} dose proposed in the literature[48] that led to excessive
444 increases in bone volume fraction (BV/TV) by the end of the experiment. The 40 µg kg^{-1} d^{-1}
445 dose was chosen to obtain BV/TV increases comparable to those observed with BIS and SclAb
446 treatments, enabling a more balanced comparison across treatment groups (see Fig. 1b).

447

448 **Bone morphometry**

449 Micro-CT images were obtained with a vivaCT 40 (Scanco Medical AG, Brüttisellen,
450 Switzerland) operated at 55 kVp and 146 µA. 1000 projection images were obtained with an
451 integration time of 200 ms. Grayscale images were reconstructed using a Feldkamp algorithm,
452 with automated beam hardening correction, resulting in an isotropic voxel size of 10.5 µm. The
453 image of week 20 was aligned in the main loading direction. Follow up scans were registered
454 to the previous scan. A constrained 3D Gauss filter (sigma 1.2, support 1) and a global
455 thresholding procedure of 22% (approximately 580 mg HA cm^{-3}) were applied. Automated
456 masks were created to extract the trabecular bone volumes (trabecular mask truncated by 10%
457 of length at both ends to exclude epiphyses and primary spongiosa; middle 26% removed

458 because this area is almost void of trabeculae)[18]. The cortical mask included 75% of the length
459 of the inner mask[18]. Static trabecular bone morphometric parameters were calculated according
460 to Bouxsein et al.[49]. Dynamic bone morphometry was performed by registering and
461 superimposing segmented bone volume images of consecutive time points. Bone formation and
462 resorption rates were calculated[36] over two two-week periods (w20-22 and w22-24).

463

464 **Finite element analysis of mechanical properties**

465 Finite-element simulations were used to analyze mechanical properties of the vertebrae. 3D
466 micro-FE models were generated by converting all voxels of the micro-CT image to 8 node
467 hexahedral elements, with each model consisting of approximately 1.8 million elements. A
468 Young's modulus of 14.8 GPa and a Poisson's ratio of 0.3[44] were assigned. Each model was
469 solved with ParOSol[50] running on the Euler cluster operated by Scientific IT Services at ETH
470 Zurich. Cylindric intervertebral disks (10% of absolute height) were applied and assigned the
471 same Young's modulus and Poisson's ratio as bone. The top of the model was displaced by 1%
472 of the total vertebral length, while the bottom was fixed. The resulting reaction force was
473 rescaled to the value of the force applied in the experimental setup; consequently, all the FE
474 outcomes were rescaled accordingly (4 N for non-loaded[46] and 8 N for loaded mice). Strain
475 energy density (SED), defined as the increase in energy associated with the tissue deformation
476 per unit volume, and effective strain were used as the mechanical signal. Trabecular bone
477 strength was estimated for each mouse at each time point by using the Pistoia criterion[51] which
478 assumes that bone failure is initiated if a certain percentage of the bone tissue (2%) is strained
479 beyond the tissue yield effective strain (7000 $\mu\varepsilon$). This criterion has been shown applicable to
480 the mouse vertebra as well[52]. For the predicted bone strength estimation, the full bone was
481 modeled but only the effective strains in the trabecular compartment were analyzed.

482

483 **Local mechanoregulation analysis**

484 The local mechanical environment was derived from micro-FE simulations of the baseline scan.
485 Here, SED is used as a mathematical term to describe the (re)modeling stimulus
486 phenomenologically. To quantify the relationship between the local SED and cellular activity
487 on the bone surface, the bone formation or resorption sites determined by rigid registration were
488 projected onto the surface of the baseline scan, resulting in three masks representing three
489 different clusters of formed (F), quiescent (Q) or resorbed (R) bone surfaces[6]. In short, the mean
490 SED value was calculated in each of these three masks and for each mouse, and normalized to
491 the mean SED of the quiescent surface as absolute SED values differ per mouse and over time
492 due to differences in BV/TV. To establish a quantitative description of the mechanoregulatory
493 system, the relation between increasing mechanical stimuli and consequent (re)modeling events
494 was assessed by calculating the relative percentage of voxels being formed, quiescent and
495 resorbed for each value of SED binned at 1% step size of the maximum SED, and assuming
496 that each (re)modeling event has the same occurrence probability (i.e., formation, resorption
497 and quiescent regions were virtually rescaled to have the same amount of voxels) to remove
498 dependencies on imbalances in the (re)modeling process due to differences between animals or
499 treatments. The conditional probabilities were fitted per animal by exponential functions.
500 Correct classification rate (CCR) values were calculated from the mean conditional
501 probabilities from all animals, returning a scalar value between 0.33 and 1 assessing overall
502 mechanoregulation, with 0.33 meaning (re)modeling is independent of the mechanical signal
503 and 1 meaning it is entirely dependent on the mechanical signal. (Re)modeling velocities
504 (RmVs) and their mechanostat parameters were calculated according to Marques et al. for each
505 animal[19]. Minimum and maximum RmV, represented as formation saturation level (FSL) and
506 resorption saturation level (RSL), as well as (re)modeling thresholds (RmTs) were extracted
507 from the resulting curves.

508

509 **Statistical methods**

510 Statistical analysis was performed using R (R, Auckland, New Zealand[53]). Data are presented
511 as group means ± standard error unless otherwise specified. P-values lower than 0.05 are
512 considered significant, statistical significance was defined as *p<0.05, **p<0.01, ***p<0.001.
513 Normality was assessed using the Shapiro-Wilk test (in R, with $\alpha = 0.05$).

514 Static morphometric and mechanical parameters of trabecular bone in the 6th caudal vertebra
515 were measured at weeks 15, 20, 22, and 24, with Δ representing the percentage change between
516 weeks 20 and 24. Two-way ANOVA followed by Tukey's post-hoc test was used to compare
517 Δw20-24. Synergy (S) or antagonism (I) between treatment and mechanical loading was
518 evaluated using the interaction term ("treatment:loading") in a linear model.

519 A synergistic effect was defined as a combined treatment response that exceeded the sum of the
520 individual effects of treatment and mechanical loading. This implies that the two interventions
521 may act through the same or facilitating biological pathways. Statistically, such synergy is
522 indicated by a significant and positive interaction term between the main effect (treatment) and
523 mechanical loading. An antagonistic effect was defined as a combined treatment response that
524 was less than the expected additive effect of treatment and mechanical loading. Statistically,
525 such antagonism was reflected by a significant and negative interaction term between the main
526 effect (treatment) and mechanical loading. The animal provider from the third (SclAB) and
527 fourth (PTH) experiment was different, therefore we adjusted the model for this.

528 Dynamic morphometric parameters were analyzed during weeks 20-22 and 22-24. One-way
529 ANOVA followed by Tukey's post-hoc test was applied to absolute values in each time interval.
530 Synergy or antagonism was assessed using the interaction term from a linear model of $\log_2$-
531 transformed values in each time interval.

Strain Energy Density (SED) in formation (F), quiescence (Q), and resorption (R) surfaces was reported for each group in each time interval. Differences between F, Q, and R were compared using two-sided Wilcoxon signed-rank tests with Bonferroni correction after testing for normality.

For conditional probabilities, exponential curves were fitted to the formation and resorption slopes. For formation, a saturating exponential model $f(x) = y_0 + a \cdot (1 - \exp(-bx))$ was applied to the first 40% of normalized SED data for each animal individually, with parameters y_0, a, and b representing level of formation in the absence of mechanical stimulus (i.e. at SED = 0), maximal formation, and sensitivity to mechanical stimulus, respectively. For resorption, a decaying exponential model $f(x) = y_0 + a \cdot \exp(-bx))$ was used to assess the rate of resorption. Resorption asymptote min_R represents the saturation level of resorption at high mechanical signal, i.e. the minimum resorption probability ($x \rightarrow \infty$), indicative of the amount of non-targeted resorption. Coefficient a represents the magnitude of the response, i.e. the difference between the initial and the minimum resorption probability. Coefficient b is the rate of decay, representing how quickly the probability of resorption drops as SED increases. Synergy or antagonism was assessed using the interaction term from a linear model applied to $\log_2$-transformed coefficients, with significance determined by two-way ANOVA followed by Tukey's post-hoc test.

Formation and resorption saturation levels (FSL, RSL) and remodeling thresholds (RmTs) were derived from hyperbola remodeling velocity curves, fitted with the function $f(x) = y_0 + \frac{a}{(b-x)}$, where x represents the mechanical signal, y_0 the FSL, and a the (re)modeling velocity modulus. The remodeling threshold (RmT) is defined as: $RmT = b + \frac{a}{y_0}$. One-way ANOVA followed by Tukey's post-hoc test was used for statistical comparisons, with synergy or antagonism assessed using the interaction term from a linear model applied to absolute values in each time interval, because FSL and RSL can obtain negative values.

Modeling and remodeling amounts were calculated by monitoring spatial agreement of voxels over the time intervals w20-22 and w22-24, following the approach presented by Birkhold *et al.*[37]. Modeling amount was defined as formation without prior resorption in either the first or the second interval, divided by the amount of surface voxels. Remodeling amount was defined as resorption followed by formation, divided by the amount of surface voxels.

Linear correlations between the %-change in predicted strength and parameter outcomes were assessed using Pearson's correlation coefficient R. For nonlinear relationships, we employed a power-law model of the form $y = a \cdot x^b$, which was linearized via logarithmic transformation to $\ln(\mathrm{y}) = \ln(a) + b \cdot \ln(x)$. Parameters a and b were estimated using linear regression on the transformed data, and the Spearman's correlation coefficient ρ between the log-transformed observed and predicted values was used to assess the goodness of fit. Since the fitted power-law model adequately described the nonlinear relationships, we did not perform a formal model selection procedure to compare alternative models, such as those based on the Akaike information criterion (AIC).

Data availability

The primary data supporting the findings of this study are available within the paper. Source data are provided with this paper. The raw data generated during the study are available in a Zenodo repository (see link below).

Code availability

All data and code are available in a Zenodo repository: 10.5281/zenodo.17256047.

580 **References**

581

582 1. Kanis JA, McCloskey EV, Johansson H, Oden A, Melton LJ, Khaltaev N. A reference
583 standard for the description of osteoporosis. *Bone* **42**, 467-475 (2008).

584

585 2. Schumm AK*, et al.* Does adding exercise or physical activity to pharmacological osteoporosis
586 therapy in patients with increased fracture risk improve bone mineral density and lower
587 fracture risk? A systematic review and meta-analysis. *Osteoporosis Int* **34**, 1867-1880 (2023).

588

589 3. Kim SW*, et al.* Sclerostin Antibody Administration Converts Bone Lining Cells Into Active
590 Osteoblasts. *Journal of Bone and Mineral Research* **32**, 892-901 (2017).

591

592 4. Duan P, Bonewald LF. The role of the wnt/beta-catenin signaling pathway in formation and
593 maintenance of bone and teeth. *Int J Biochem Cell Biol* **77**, 23-29 (2016).

594

595 5. Kim JM, Lin C, Stavre Z, Greenblatt MB, Shim JH. Osteoblast-Osteoclast Communication
596 and Bone Homeostasis. *Cells* **9**, (2020).

597

598 6. Schulte FA*, et al.* Local mechanical stimuli regulate bone formation and resorption in mice at
599 the tissue level. *PLoS One* **8**, e62172 (2013).

600

601 7. Dell RM*, et al.* Incidence of atypical nontraumatic diaphyseal fractures of the femur. *J Bone*
602 *Miner Res* **27**, 2544-2550 (2012).

603

604 8. Kulkarni NH*, et al.* Effects of parathyroid hormone on Wnt signaling pathway in bone. *J Cell*
605 *Biochem* **95**, 1178-1190 (2005).

606

607 9. Sugiyama T*, et al.* Mechanical loading enhances the anabolic effects of intermittent
608 parathyroid hormone (1-34) on trabecular and cortical bone in mice. *Bone* **43**, 238-248 (2008).

609

610 10. Rooney AM, McNeill TJ, Ross FP, Bostrom MPG, van der Meulen MCH. PTH Treatment
611 Increases Cortical Bone Mass More in Response to Compression than Tension in Mice.
612 *Journal of Bone and Mineral Research* **38**, 59-69 (2023).

613

614 11. Baron R, Kneissel M. WNT signaling in bone homeostasis and disease: from human
615 mutations to treatments. *Nat Med* **19**, 179-192 (2013).

616

617 12. Ominsky MS, Boyce RW, Li X, Ke HZ. Effects of sclerostin antibodies in animal models of
618 osteoporosis. *Bone* **96**, 63-75 (2017).

619

620 13. Robling AG*, et al.* Mechanical stimulation of bone in vivo reduces osteocyte expression of
621 Sost/sclerostin. *J Biol Chem* **283**, 5866-5875 (2008).

622

14. Rauner M, Taipaleenmaki H, Tsourdi E, Winter EM. Osteoporosis Treatment with Anti-Sclerostin Antibodies-Mechanisms of Action and Clinical Application. *J Clin Med* **10**, (2021).

15. Frost HM. The mechanostat: a proposed pathogenic mechanism of osteoporoses and the bone mass effects of mechanical and nonmechanical agents. *Bone Miner* **2**, 73-85 (1987).

16. Frost HM. Bone "mass" and the "mechanostat": a proposal. *Anat Rec* **219**, 1-9 (1987).

17. Frost HM. Bone's mechanostat: a 2003 update. *Anat Rec A Discov Mol Cell Evol Biol* **275**, 1081-1101 (2003).

18. Lambers FM, Schulte FA, Kuhn G, Webster DJ, Müller R. Mouse tail vertebrae adapt to cyclic mechanical loading by increasing bone formation rate and decreasing bone resorption rate as shown by time-lapsed in vivo imaging of dynamic bone morphometry. *Bone* **49**, 1340-1350 (2011).

19. Marques FC, Boaretti D, Walle M, Scheuren AC, Schulte FA, Müller R. Mechanostat parameters estimated from time-lapsed micro-computed tomography data of mechanically driven bone adaptation are logarithmically dependent on loading frequency. *Front Bioeng Biotech* **11**, (2023).

20. Christen P*, et al.* Bone remodelling in humans is load-driven but not lazy. *Nat Commun* **5**, 4855 (2014).

21. Griesbach JK, Schulte FA, Schadli GN, Rubert M, Müller R. Mechanoregulation analysis of bone formation in tissue engineered constructs requires a volumetric method using time-lapsed micro-computed tomography. *Acta Biomater*, (2024).

22. Taylor S*, et al.* Time-dependent cellular and transcriptional changes in the osteoblast lineage associated with sclerostin antibody treatment in ovariectomized rats. *Bone* **84**, 148-159 (2016).

23. Ominsky MS*, et al.* Romosozumab Improves Bone Mass and Strength While Maintaining Bone Quality in Ovariectomized Cynomolgus Monkeys. *Journal of Bone and Mineral Research* **32**, 788-801 (2017).

24. Morse A, Schindeler A, McDonald MM, Kneissel M, Kramer I, Little DG. Sclerostin Antibody Augments the Anabolic Bone Formation Response in a Mouse Model of Mechanical Tibial Loading. *J Bone Miner Res* **33**, 486-498 (2018).

25. Morse A*, et al.* Mechanical load increases in bone formation via a sclerostin-independent pathway. *J Bone Miner Res* **29**, 2456-2467 (2014).

26. Witcher PC*, et al.* Sclerostin neutralization unleashes the osteoanabolic effects of Dkk1 inhibition. *Jci Insight* **3**, (2018).

27. Morse A*, et al.* KO Mice Treated with Sclerostin Antibody Have Additional Increases in Bone Volume. *Calcified Tissue Int* **103**, 298-310 (2018).

28. Florio M*, et al.* A bispecific antibody targeting sclerostin and DKK-1 promotes bone mass accrual and fracture repair. *Nature Communications* **7**, (2016).

29. Ryder KD, Duncan RL. Parathyroid hormone modulates the response of osteoblast-like cells to mechanical stimulation. *Calcif Tissue Int* **67**, 241-246 (2000).

30. Hagino H, Okano T, Akhter MP, Enokida M, Teshima R. Effect of parathyroid hormone on cortical bone response to in vivo external loading of the rat tibia. *J Bone Miner Metab* **19**, 244-250 (2001).

31. Robinson ST, Shyu PT, Guo XE. Mechanical loading and parathyroid hormone effects and synergism in bone vary by site and modeling/remodeling regime. *Bone* **153**, 116171 (2021).

32. Uusi-Rasi K*, et al.* Effect of alendronate and exercise on bone and physical performance of postmenopausal women: a randomized controlled trial. *Bone* **33**, 132-143 (2003).

33. Kistler-Fischbacher M, Yong JS, Weeks BK, Beck BR. A Comparison of Bone-Targeted Exercise With and Without Antiresorptive Bone Medication to Reduce Indices of Fracture Risk in Postmenopausal Women With Low Bone Mass: The MEDEX-OP Randomized Controlled Trial. *J Bone Miner Res* **36**, 1680-1693 (2021).

34. Sims NA, Martin TJ. Osteoclasts Provide Coupling Signals to Osteoblast Lineage Cells Through Multiple Mechanisms. *Annu Rev Physiol* **82**, 507-529 (2020).

35. Birkhold AI, Razi H, Duda GN, Weinkamer R, Checa S, Willie BM. Mineralizing surface is the main target of mechanical stimulation independent of age: 3D dynamic in vivo morphometry. *Bone* **66**, 15-25 (2014).

36. Schulte FA, Lambers FM, Kuhn G, Müller R. In vivo micro-computed tomography allows direct three-dimensional quantification of both bone formation and bone resorption parameters using time-lapsed imaging. *Bone* **48**, 433-442 (2011).

37. Birkhold AI, Razi H, Weinkamer R, Duda GN, Checa S, Willie BM. Monitoring in vivo (re)modeling: a computational approach using 4D microCT data to quantify bone surface movements. *Bone* **75**, 210-221 (2015).

38. Acevedo C, Stadelmann VA, Pioletti DP, Alliston T, Ritchie RO. Fatigue as the missing link between bone fragility and fracture. *Nat Biomed Eng* **2**, 62-71 (2018).

39. Hernandez CJ, Lambers FM, Widjaja J, Chapa C, Rimnac CM. Quantitative relationships between microdamage and cancellous bone strength and stiffness. *Bone* **66**, 205-213 (2014).

40. Lambers FM, Bouman AR, Rimnac CM, Hernandez CJ. Microdamage caused by fatigue loading in human cancellous bone: relationship to reductions in bone biomechanical performance. *PLoS One* **8**, e83662 (2013).

41. Mathavan N*, et al.* Spatial transcriptomics in bone mechanomics: Exploring the mechanoregulation of fracture healing in the era of spatial omics. *Sci Adv* **11**, eadp8496 (2025).

42. Duda GN, Geissler S, Checa S, Tsitsilonis S, Petersen A, Schmidt-Bleek K. The decisive early phase of bone regeneration. *Nat Rev Rheumatol* **19**, 78-95 (2023).

43. Lambers FM, Kuhn G, Schulte FA, Koch K, Müller R. Longitudinal assessment of in vivo bone dynamics in a mouse tail model of postmenopausal osteoporosis. *Calcif Tissue Int* **90**, 108-119 (2012).

44. Webster DJ, Morley PL, van Lenthe GH, Müller R. A novel in vivo mouse model for mechanically stimulated bone adaptation--a combined experimental and computational validation study. *Comput Methods Biomech Biomed Engin* **11**, 435-441 (2008).

45. Scheuren AC*, et al.* Mechano-Regulation of Trabecular Bone Adaptation Is Controlled by the Local in vivo Environment and Logarithmically Dependent on Loading Frequency. *Front Bioeng Biotechnol* **8**, 566346 (2020).

46. Christen P, van Rietbergen B, Lambers FM, Muller R, Ito K. Bone morphology allows estimation of loading history in a murine model of bone adaptation. *Biomech Model Mechanobiol* **11**, 483-492 (2012).

47. Stadelmann VA, Bonnet N, Pioletti DP. Combined effects of zoledronate and mechanical stimulation on bone adaptation in an axially loaded mouse tibia. *Clin Biomech (Bristol, Avon)* **26**, 101-105 (2011).

48. Alexander JM*, et al.* Human parathyroid hormone 1-34 reverses bone loss in ovariectomized mice. *J Bone Miner Res* **16**, 1665-1673 (2001).

49. Bouxsein ML, Boyd SK, Christiansen BA, Guldberg RE, Jepsen KJ, Müller R. Guidelines for Assessment of Bone Microstructure in Rodents Using Micro-Computed Tomography. *Journal of Bone and Mineral Research* **25**, 1468-1486 (2010).

50. Flaig C, Arbenz P. A scalable memory efficient multigrid solver for micro-finite element analyses based on CT images. *Parallel Comput* **37**, 846-854 (2011).

51. Pistoia W, Van Rietbergen B, Lochmüller EM, Lill CA, Eckstein F, Rüegsegger P. Estimation of distal radius failure load with micro-finite element analysis models based on three-dimensional peripheral quantitative computed tomography images. *Bone* **30**, 842-848 (2002).

52. Nyman JS, *et al.* Predicting mouse vertebra strength with micro-computed tomography-derived finite element analysis. *Bonekey Rep* **4**, 664 (2015).

53. Team RDC. R: A language and environment for statistical computing. . In: *R Foundation for Statistical Computing*) (2007).

Acknowledgements

We acknowledge Kathleen Koch for assistance and performance of animal experiments of the PTH and BIS groups, and Dr. Ulrike Kettenberger for assistance and performance of animal experiments of the PTH group. Nirujan Pasupathy and Júlia van den Nest Molina have supported the analyses of modeling and mechanoregulation mechanisms. This work was funded by the European Union grant VPHOP (FP7-ICT-2008-223865; FAS, FML, CW, GAK) and the European Research Council ERC Advanced grant (MechAGE ERC-2016-ADG-741883; FCM, GAK).

Author contributions

RM, GAK, PJR designed the experiment. CW, GAK, MS, FML performed the experiments. FAS, FCM, JG, CW, MS, FML, GAK performed image processing and analysis. MK provided pharmacological agents. RM, GAK, PJR, CK supervised the project. FAS wrote the original draft of the manuscript. All authors contributed to data interpretation, were involved in discussions throughout the study, and participated in manuscript revision and preparation.

Competing interests

MK, PJR, and CK are employees of Novartis. The other authors declare they have no competing interests.

Figure legends

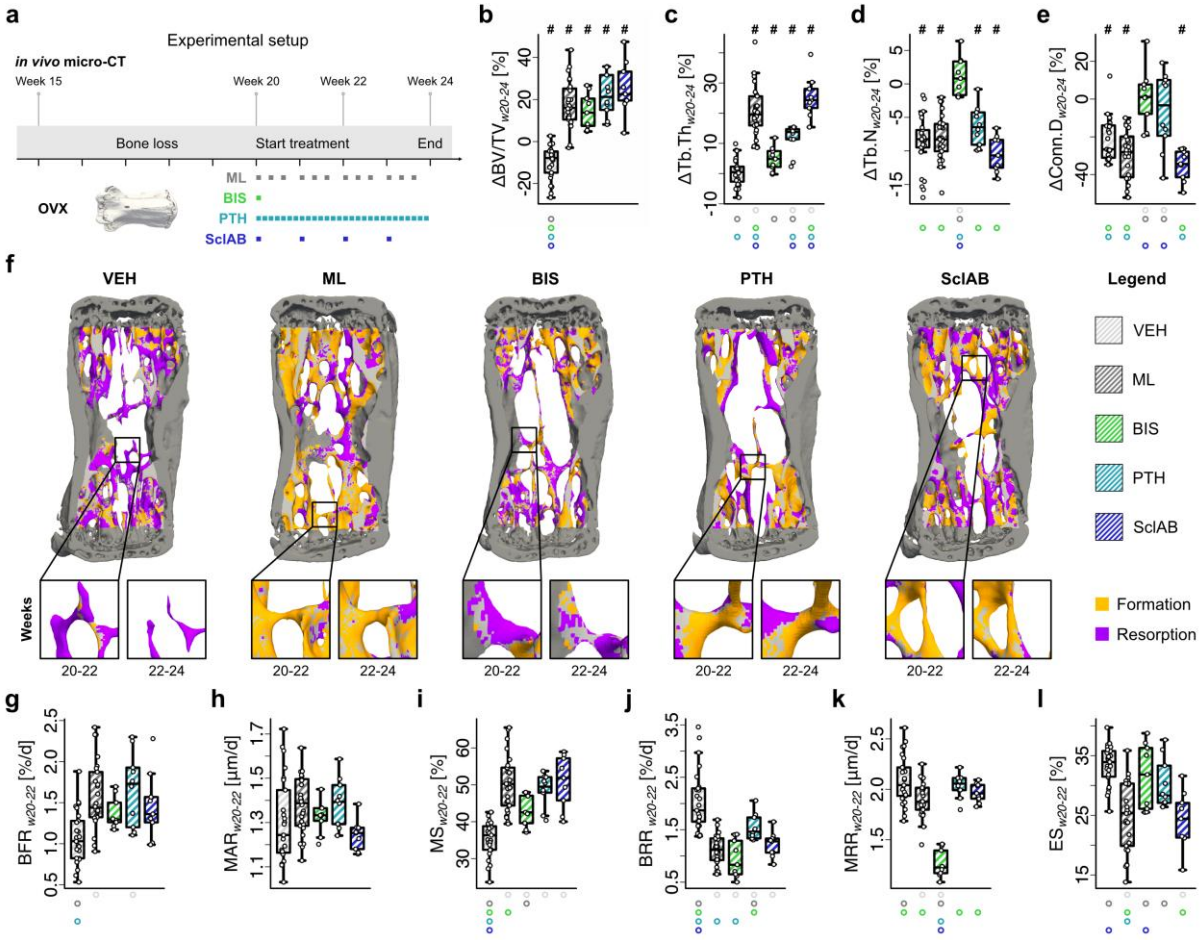

Figure 1: Osteoporosis monotreatments enhance trabecular bone micro-architecture by different mechanisms of action. *(**a**) Experimental setup. 15-week-old mice are ovariectomized, and treatment is administered between week 20 (w20) and 24 (w24). (**b-e, g-l**) Monotreatments (VEH: n=25, BIS: n=9, PTH: n=10, SclAB: n=9; each data point represents one animal (biological replicate)), boxplots show percentage change. The box spans the interquartile range (IQR) from the 25th to the 75th percentile. The median is shown as a line inside the box. Whiskers extend to the most extreme data points within 1.5 × IQR, points beyond this range are plotted as outliers. # indicates that the delta of the group is different from zero, as tested with t-test with null-hypothesis. (**b**) bone volume fraction ΔBV/TV, (**c**) trabecular thickness ΔTb.Th, (**d**) trabecular number ΔTb.N (**e**) connectivity density ΔConn.D. (**f**) Representative micro-computed tomography overlays at intervals w20-22 and w22-24, with formation and resorption volumes (**g-l**) (Re)modeling rates calculated from time interval w20-22 (**g**) bone formation rate per bone volume BFR (**h**) mineral apposition rate MAR (**i**) mineralizing surface per bone surface MS (**j**) bone resorption rate per bone volume BRR (**k**) mineral resorption rate MRR (**l**) eroded surface per bone surface ES. Significant differences are depicted with a symbol in the color of the corresponding group (o: to monotreatment, ●: to combined treatment, see Supplementary Table S.1 for color encoding, p<0.05). Source data are provided as a Source Data file.*

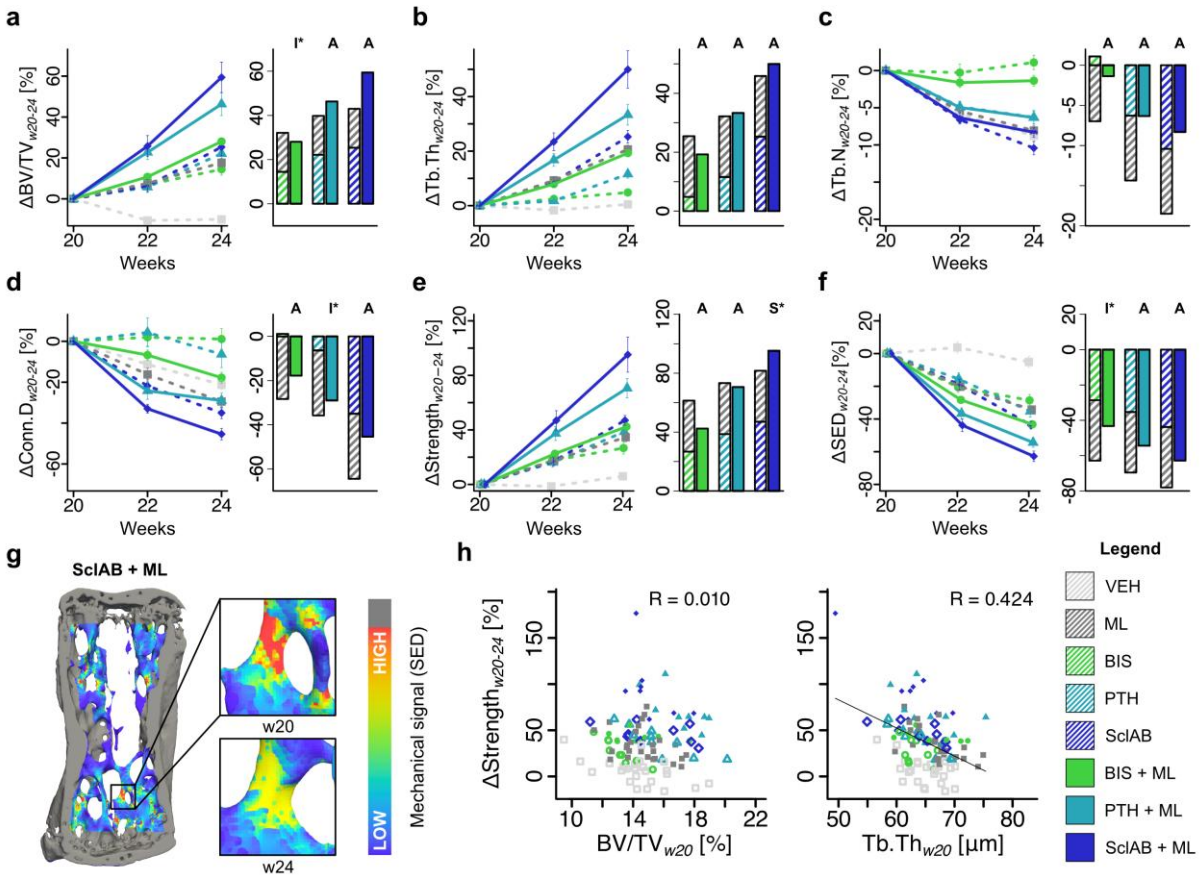

Figure 2: Mechanical loading increases the morphological effects of anabolic and anti-catabolic treatments, contributing to increased predicted strength. *(**a-f**) Changes from baseline. Data are presented as mean ± standard error. Each data point represents one animal (biological replicate; VEH: n=25, ML: n=26, BIS: n=9, BIS +ML: n=9, PTH: n=10, PTH +ML: n=9, ScIAB: n=9, ScIAB +ML: n=8) **(a)** bone volume fraction (ΔBV/TV) **(b)** trabecular thickness (ΔTb.Th) **(c)** trabecular number (ΔTb.N) **(d)** connectivity density (ΔConn.D) **(e)** predicted strength (ΔStrength), and **(f)** strain energy density (ΔSED). Bars show group means of sum of single vs. combined treatment indicating: antagonistic (I), additive (A) or synergistic (S) effects determined via treatment:loading interaction in a linear model on the %-change. **(g)** Example of SED distribution in the 6th caudal vertebra of a ScIAB + ML animal at week 20, showing reduced SED after structural reorganization from week 20 to 24. **(h)** Linear regression of ΔStrength with BV/TV and Tb.Th at week 20. Source data are provided as a Source Data file.*

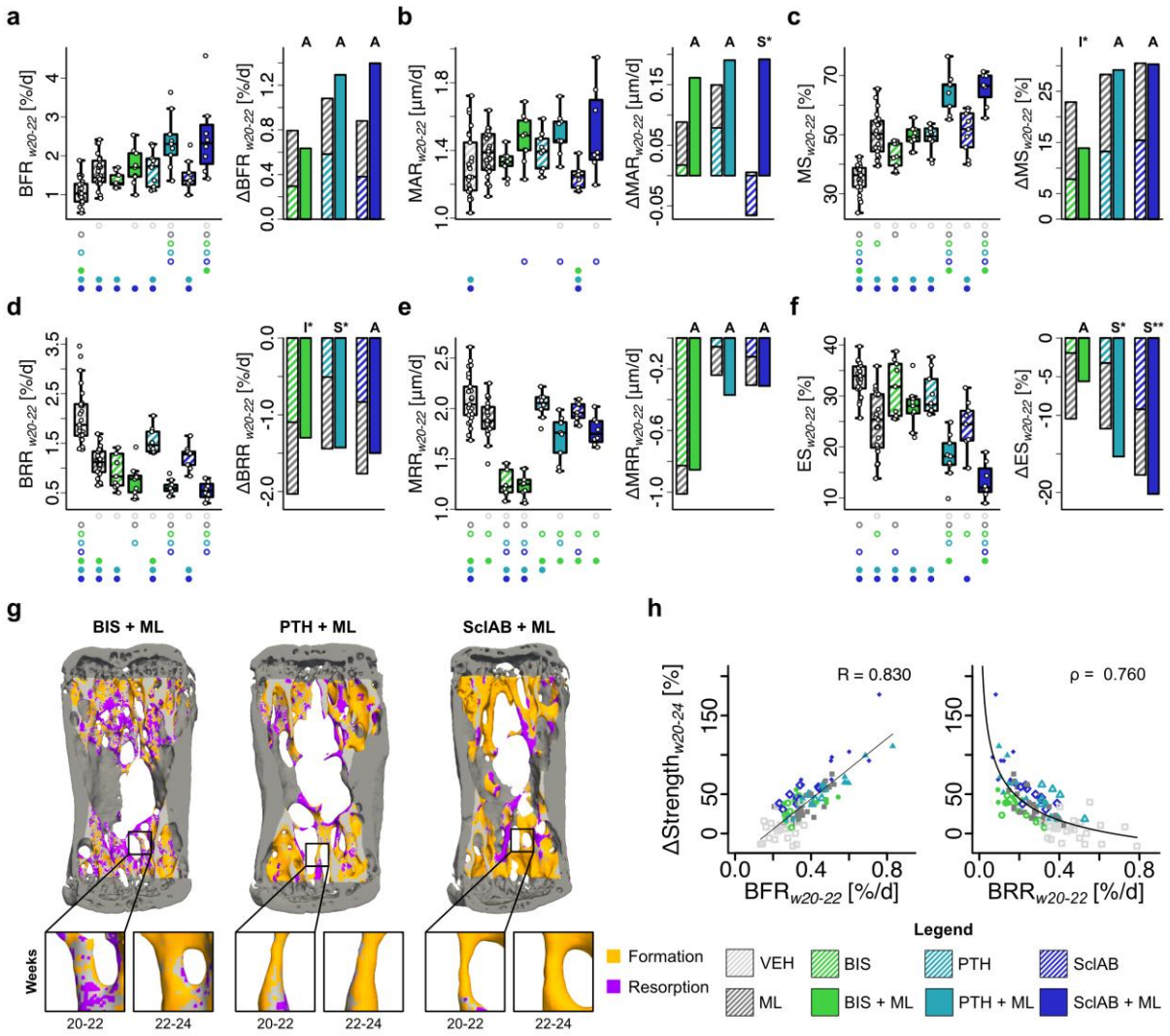

***Figure 3**: **Mechanical loading increases bone formation and decreases resorption rates of anabolic and anti-catabolic pharmacological treatments which contribute to increased predicted strength.** (**a**) bone formation rate per bone volume (BFR) (**b**) mineral apposition rate (MAR) (**c**) mineralizing surface per bone surface (MS) (**d**) bone resorption rate per bone volume (BRR) (**e**) mineral resorption rate (MRR) (**f**) eroded surface per bone surface (ES). **(a-f)** Each data point represents one animal (biological replicate; VEH: n=25, ML: n=26, BIS: n=9, BIS +ML: n=9, PTH: n=10, PTH +ML: n=9, SclAB: n=9, SclAB +ML: n=8). The box spans the interquartile range (IQR) from the 25th to the 75th percentile. The median is shown as a line inside the box. Whiskers extend to the most extreme data points within 1.5 × IQR, points beyond this range are plotted as outliers. Δ denotes difference from VEH as no baseline value for dynamic bone morphometry rates was available. Bars show group means of sum of single vs. combined treatment indicating: antagonistic (I), additive (A) or synergistic (S) effects determined via treatment:loading interaction in a linear model on the log_2-transformed values. Significances were calculated using one-way ANOVA followed by Tukey's post-hoc test; significant differences are depicted with a symbol in the color of the corresponding group (o: to monotreatment, ●: to combined treatment, see Supplementary Table S.1 for color encoding, $p<0.05$). (**g**) Visual representations of combination groups BIS + ML, PTH + ML, and SclAB + ML in week intervals w20-22*

*and w22-24 (**h**) Linear regression of ΔStrength with BFR, and exponential regression analysis with BRR in week interval w20-22. Source data are provided as a Source Data file.*

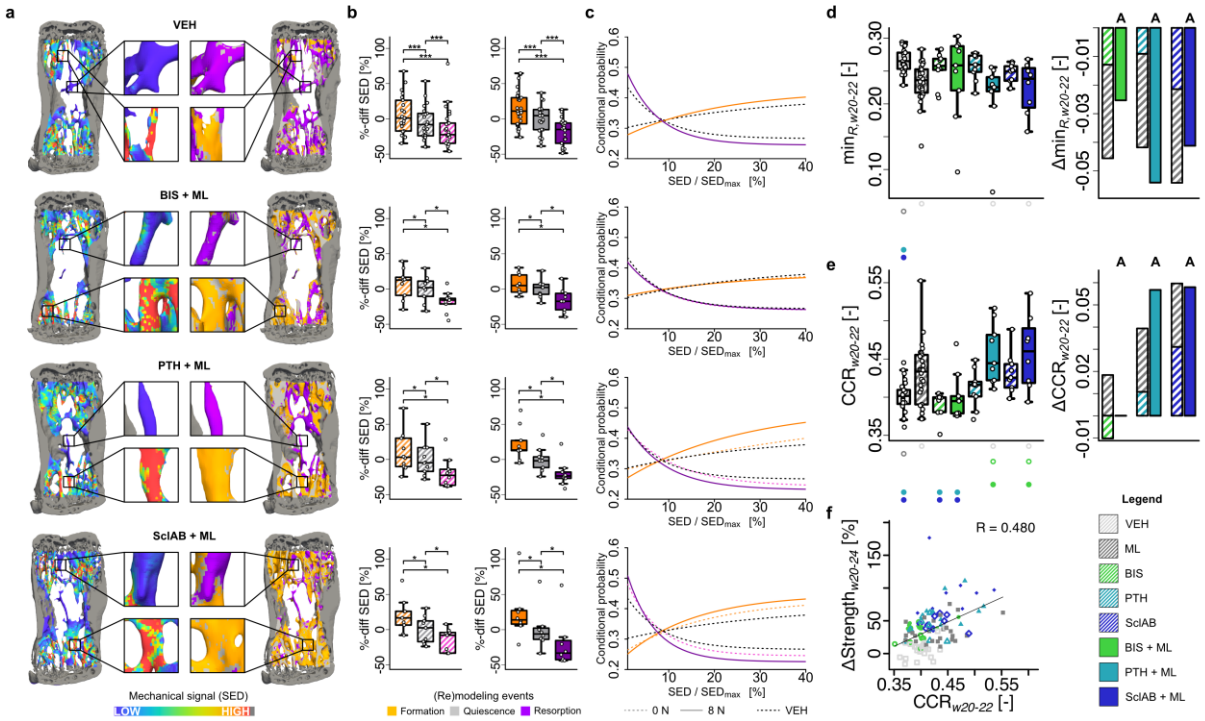

***Figure 4: Formation aligns with high mechanical signal, resorption with low**: **(a)** Spatial comparison of local mechanical signal (SED at week 20) with sites of trabecular bone formation and resorption (w20-22). **(b)** SED at formation, resorption, and quiescent sites[6], normalized to the group mean of quiescence to allow statistical testing with this group. Each data point represents one animal (biological replicate; VEH: n=25, ML: n=26, BIS: n=9, BIS +ML: n=9, PTH: n=10, PTH +ML: n=9, SclAB: n=9, SclAB +ML: n=8). The box spans the interquartile range (IQR) from the 25th to the 75th percentile. The median is shown as a line inside the box. Whiskers extend to the most extreme data points within 1.5 × IQR, points beyond this range are plotted as outliers. *p<0.05, ***<0.001 using two-sided paired Wilcoxon-signed rank test with Bonferroni correction; exact p-values are found in Supplementary Table S.6. **(c)** The plots show the exponential fitting functions (taking all animals per group into account) for conditional probability of formation and resorption as a function of SED/SED$_{max}$. Dashed lines represent monotreatment (0N, including VEH), and solid lines represent combined treatment with mechanical loading (8N, including ML). VEH is indicated by black dotted line. Values are cropped above 40% due to* low voxel count[6]. ***(d-e)** Each data point represents one animal (biological replicate; VEH: n=25, ML: n=26, BIS: n=9, BIS +ML: n=9, PTH: n=10, PTH +ML: n=9, SclAB: n=9, SclAB +ML: n=8). The box spans the interquartile range (IQR) from the 25th to the 75th percentile. The median is shown as a line inside the box. Whiskers extend to the most extreme data points within 1.5 × IQR, points beyond this range are plotted as outliers. [-] denotes unitless, Δ denotes change from VEH; sum of single vs. combined treatment group means indicating antagonistic (I), additive (A) or synergistic (S) effects. **(d)** Asymptotic resorption probability value (min$_R$). **(e)** CCR as a measure of mechanoregulated (re)modeling, with the ΔCCR bar for the BIS + ML group close to zero, making it barely visible. **(f)** Linear regression analysis in week interval w20-22 of ΔStrength with CCR.*

845 *Significant differences are depicted with a symbol in the color of the corresponding group (o: to monotreatment, ●: to*
846 *combined treatment, see Supplementary Table S.1 for color encoding, p<0.05). Source data are provided as a Source Data*
847 *file.*

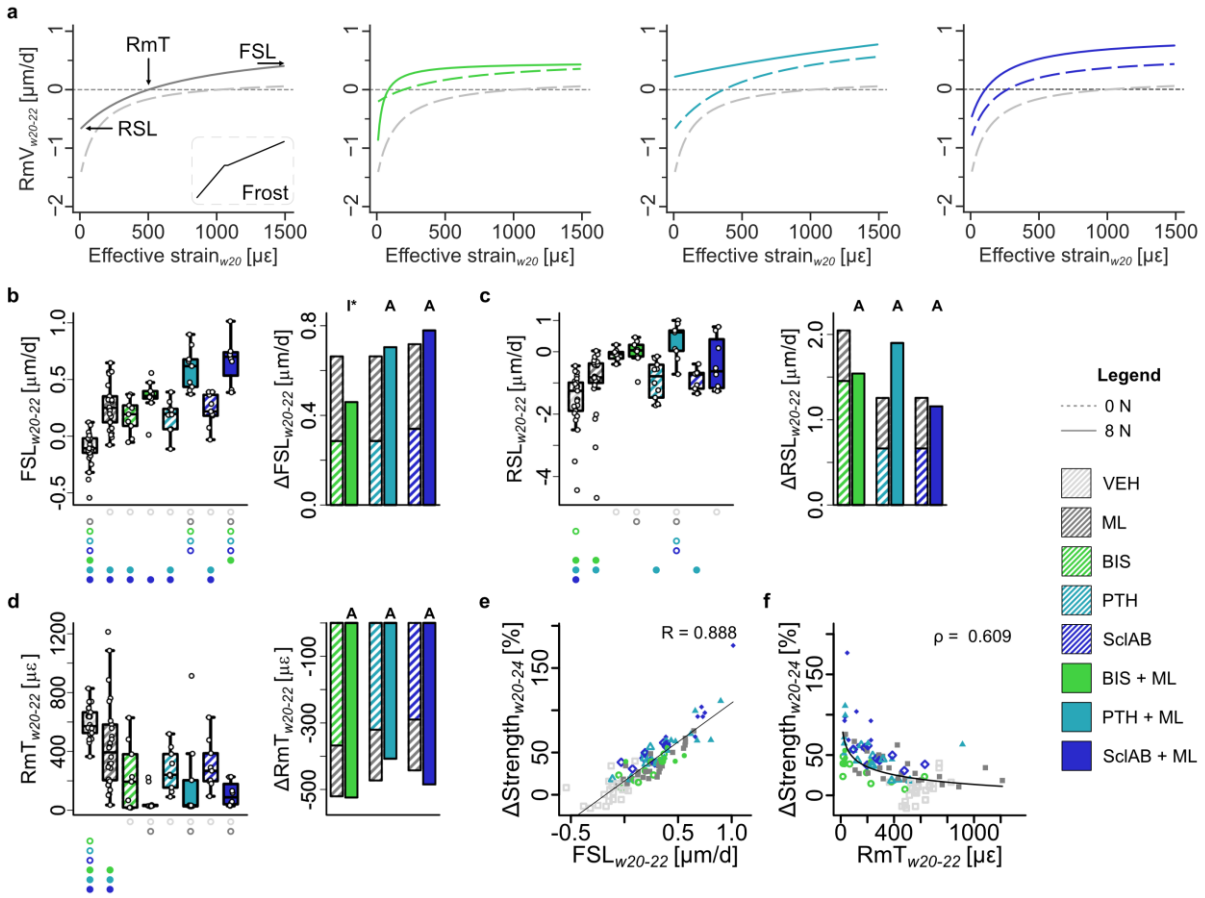

848

849 ***Figure 5: (Re)modeling velocity curves as an approximation of the mechanostat theory. (a)*** *(re)modeling velocity (RmV)*
850 *curve fits (taking all animals per group into account) for VEH / ML, BIS / BIS + ML, PTH / PTH + ML, SclAB / SclAB + ML;*
851 ***(b)*** *formation saturation level (FSL)* ***(c)*** *resorption saturation level (RSL),* ***(d)*** *(re)modeling threshold (RmT)* ***(b-d)*** *Each data*
852 *point represents one animal (biological replicate; VEH: n=25, ML: n=26, BIS: n=9, BIS +ML: n=9, PTH: n=10, PTH +ML:*
853 *n=9, SclAB: n=9, SclAB +ML: n=8). The box spans the interquartile range (IQR) from the 25th to the 75th percentile. The*
854 *median is shown as a line inside the box. Whiskers extend to the most extreme data points within 1.5 × IQR, points beyond this*
855 *range are plotted as outliers. Δ denotes difference from VEH as no baseline value from week 20 was available. Bars show*
856 *group means of sum of single vs. combined treatment indicating: antagonistic (I), additive (A) or synergistic (S) effects*
857 *determined via treatment:loading interaction in a linear model on the absolute values. Significances were calculated using*
858 *one-way ANOVA followed by Tukey's post-hoc test; significant differences are depicted with a symbol in the color of the*
859 *corresponding group (o: to monotreatment, ●: to combined treatment, see Supplementary Table S.1 for color encoding,*
860 *p<0.05).* ***(e)*** *Linear regression of ΔStrength with FSL, and* ***(f)*** *power-law regression with RmT from week interval w20-22.*
861 *Source data are provided as a Source Data file.*

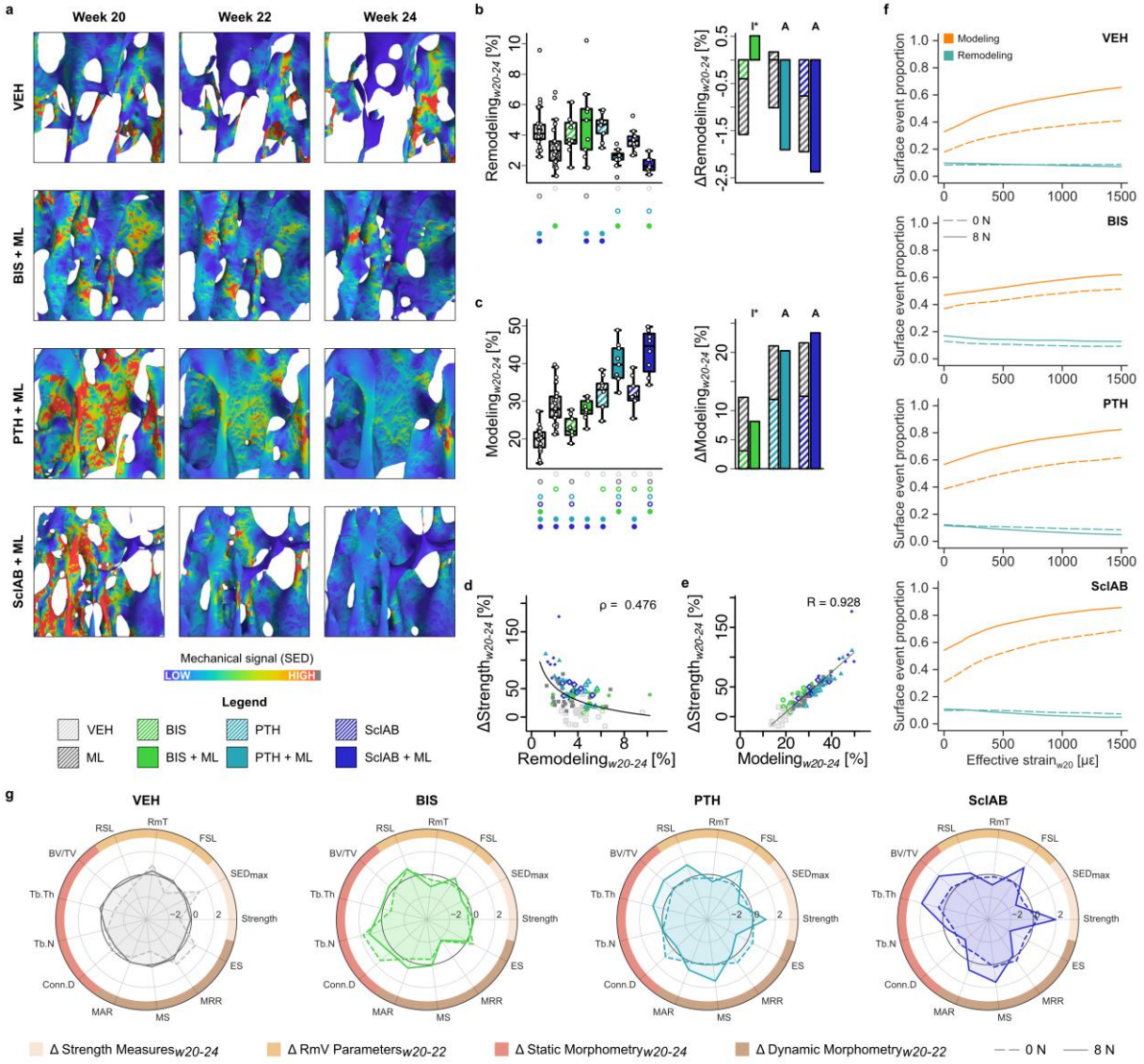

Figure 6: Modeling capacity correlates highly with the increase in predicted strength. ***(a)*** *Heterogeneity of the strain distribution decreases to different extents in different treatments. Qualitative comparison of changing SED-distribution for VEH, BIS + ML, PTH + ML and SclAB + ML over the course of 4 weeks of treatment.* ***(b)*** *Remodeling as calculated from formation following resorption at the same location over 3 measurement time points (w20, w22, w24).* ***(c)*** *Modeling as calculated from formation following quiescence at the same location over 3 measurement time points (w20, w22, w24)* ***(b-c)*** *Each data point represents one animal (biological replicate; VEH: n=25, ML: n=26, BIS: n=9, BIS +ML: n=9, PTH: n=10, PTH + ML: n=9, SclAB: n=9, SclAB + ML: n=8). The box spans the interquartile range (IQR) from the 25th to the 75th percentile. The median is shown as a line inside the box. Whiskers extend to the most extreme data points within 1.5 × IQR, points beyond this range are plotted as outliers. Δ denotes change from VEH; sum of single vs. combined treatment group means indicating graphically antagonistic (I), additive (A) or synergistic (S) effects. Significant differences are depicted with a symbol in the color of the corresponding group (o: to monotreatment, ●: to combined treatment, see Supplementary Table S.1 for color encoding, p<0.05).* ***(d)*** *Remodeling amount in % correlated to increases in predicted strength fitted using a power-law function.* ***(e)*** *Modeling amount in % correlated to increases in predicted strength fitted using linear regression.* ***(f)*** *Surface*

event proportion (modeling or remodeling) in relation to the mechanical signal. ***(g)*** *Spider plots summarizing the mean of outcome parameters of the analyzed treatments. Values were standardized to facilitate visual comparisons between groups. Source data are provided as a Source Data file.*